Dissolution-reprecipitation and self-assembly of serpentine nanoparticles preceding chrysotile formation: Insights into the structure of proto-serpentine

ROMAIN LAFAY[1,2,*], ALEJANDRO FERNANDEZ-MARTINEZ[1,3], GERMAN MONTES-HERNANDEZ[1,3], ANNE LINE AUZENDE[1], AND AGNIESZKA POULAIN[4]

[1]Universite Grenoble Alpes, ISTerre, F-38041 Grenoble, France
[2]Institute of Earth Sciences, University of Lausanne, CH-1015 Lausanne, Switzerland
[3]CNRS, ISTerre, F-38041 Grenoble, France
[4]ESRF, 71, Avenue des Martyrs, 38043 Grenoble, France

ABSTRACT

Any poorly crystalline serpentine-type mineral with a lack of recognizable textural or diffraction features for typical serpentine varieties (i.e., chryotile, lizardite, and antigorite) is usually referred to as proto-serpentine. The formation of the so-called proto-serpentine seems ubiquitous in serpentinization reactions. It is related to dissolution-precipitation of strongly reactive particles prior to true serpentine formation (e.g., in veins where both chrysotile and proto-serpentine are described). However, the structural characteristics of proto-serpentine and its relation with serpentine crystalline varieties remain unclear. In this study a model describing the transformation from proto-serpentine to chrysotile is presented based on experimental chrysotile synthesis using thermogravimetric analyses, transmission electron microscopy, and high-energy X-ray diffraction with pair distribution function analyses. The combination of the high-resolution TEM and high-energy X-ray diffraction enables to resolve the local order of neo-formed particles and their structuration processes occurring during pure chrysotile formation (i.e., during the first three hours of reaction). The formation of individual nanotubes is preceded by the formation of small nanocrystals that already show a chrysotile short-range order, forming porous anastomosing features of hydrophilic crystallites mixed with brucite. This is followed by a hierarchical aggregation of particles into a fiber-like structure. These flake-like particles subsequently stack forming concentric layers with the chrysotile structure. Finally, the individualization of chrysotile nanotubes with a homogeneous distribution of diameter and lengths (several hundreds of nanometer in length) is observed. The competitive precipitation of brucite and transient serpentine during incipient serpentinization reaction indicates that both dissolution-precipitation and serpentine-particle aggregation processes operate to form individual chrysotile. This study sheds light into mineralization processes and sets a first milestone toward the identification of the factors controlling polymorph selection mechanisms in this fascinating system.

Keywords: Proto-serpentine, pair distribution function, chrysotile, stacking, simulation

INTRODUCTION

Serpentine is a common mineral containing structural water with an ideal chemical formula $Mg_3Si_2O_5(OH)_4$. The serpentine group of minerals contains different varieties, among which the most commons forms are antigorite, consisting of periodic modulated layers (Kunze 1956), lizardite, consisting of flat periodic layers (Wicks and O'Hanley 1988), and chrysotile and polygonal serpentine, consisting in fibers (Yada 1967; Middleton and Whittaker 1976). Serpentines are mainly found in altered Earth oceanic lithosphere. Lizardite and chrysotile are both involved in hydrothermal systems and are found in the same stability domains (moderate temperature, bellow 400 °C), whereas antigorite is the high-pressure and high-temperature serpentine variety (Evans et al. 1976; Evans 2004; Wunder and Schreyer 1997). Chrysotile

is one of the most common and studied cylindrical fibrous serpentine and consists in the succession of tetrahedral sheets inserted between brucite-type magnesian octahedral layers. The structural misfit between tetrahedral and octahedral sheets induces a concentric or spiral curvature around the *x* or *y* axis (Whittaker 1956b, 1956c, 1956a; Middleton and Whittaker 1976) with a fivefold symmetry (Cressey and Whittaker 1993; Cressey et al. 2010) and with the tetrahedral sheet inside (Pauling 1930). Chrysotile is considered as a thermodynamically metastable serpentine variety having a strong chemical reactivity toward the formation of lizardite, even in the pure Mg system (Grauby et al. 1998; Evans 2004). The relationships between layered and tubular serpentine minerals, the overlap between individual polymorphs and the frequent occurrence of turbostratism in serpentine minerals (Trittschack et al. 2012) are of great interest in natural settings where both lizardite and chrysotile coexist. Moreover, an advanced understanding of the atomic scale mineral transformation mechanisms in the serpentine system remains

necessary to understand mobile elements or trace-metals cycle during oceanic lithosphere alteration.

While the structure of well-crystallized serpentine varieties has been determined from X-ray and electron diffraction and transmission electron microscopy (TEM), proto-serpentine is increasingly described as poorly crystalline serpentine precursor of undetermined fibrous serpentines in experimental (Dufaud et al. 2009; Bloise et al. 2012; Godard et al. 2013; Lafay et al. 2013) and natural (Andreani et al. 2008, 2004; Plümper et al. 2012) systems, especially in association with chrysotile. Chrysotile is generally present in supersaturated systems and veins. In this context, the alteration of mantle-silicate minerals by hydrothermal fluids is usually characterized by the development of cracks filled with serpentine or by pseudomorphic polycrystalline serpentine features originated from dissolution/precipitation processes (Wicks and Whittaker 1977; Putnis 2002). The dissolution of mantle silicate (pyroxene and olivine) appears largely controlled by its crystallographic orientation and fluid composition (Velbel 1993, 2009; Daval et al. 2010, 2013) but, to our knowledge, the direct relation between dissolution properties (e.g., rate, mechanisms) and secondary phase precipitation has never been explored. However, the formation of serpentine mineral precursors to chrysotile, which subsequently recrystallize into lizardite, is probably taking place in reaction rims at fluid-mineral interfaces and is surely linked to surface reactivity.

During the last decades various experimental studies have attempted to reproduce natural serpentinization features and to ascertain the main parameters controlling serpentinization processes (Seyfried and Dibble 1980; Macleod et al. 1994; James et al. 2003; Seyfried et al. 2007; McCollom and Bach 2009; Hövelmann et al. 2011). In this way, serpentine phase's stability domains are continuously refined. Moreover, serpentine synthesis methods, especially for chrysotile, have been developed since the mid of the last century (Noll 1950; Yada and Iishi 1974, 1977). Recent research has attempted to develop more efficient synthesis protocols and to characterize the effect of foreign elements on the mineral growth processes (Bloise et al. 2009; Korytkova and Pivovarova 2010; Korytkova et al. 2011; Lafay et al. 2014b). Some of these studies have also aimed to get a better understanding of structural factors governing natural chrysotile health hazards (Falini et al. 2006; Foresti et al. 2009; Turci et al. 2011).

The transformation from precursor phases (aqueous, colloidal, or solid) to mineral structures and the relation between mineral polymorphs is currently a very active research area in the (bio)geosciences (De Yoreo et al. 2015). However, until now very few studies have been devoted to the identification of the first steps of serpentine nucleation and growth at laboratory scale, and many questions still remain unanswered concerning the transition from the so-called proto-serpentine to crystalline serpentine. In a previous contribution we highlighted that chrysotile synthesis at 300 °C was characterized by the initial formation of a poorly crystallized serpentine associated with brucite. Here we showed that the competitive precipitation of brucite and serpentine, progressively consumed via dissolution precipitation processes, preceded the individualization and growth of single chrysotile nanotubes via a progressive Ostwald ripening process (Lafay et

al. 2013). The dissolution-precipitation process was effective during the first 20 h of reaction. The broad X-ray diffraction peaks in the diffraction pattern of the serpentine precursor crystallites (first 2 h of reaction) is surely due to small coherent domain sizes, and also probably to turbostatic disorder along the stacking direction, and to an amorphous component difficult to be interpreted from laboratory X-ray data. In summary, dissolution re-precipitation processes could be systematically involved in the transformation from proto-serpentine to the final crystalline varieties (Jancar and Suvorov 2006; Lafay et al. 2013).

In this study we expand on the efforts to decipher the nature of the amorphous and nanocrystalline phases precursors that can be formed during the early steps of chrysotile formation. For that purpose, this experimental study was based on an accurate sampling period (0.5 h) during the first steps of chrysotile synthesis (i.e., the first 3 h). A combination of thermogravimetric, TEM, and high-energy X-ray diffraction experiments, including pair distribution function analyses, were performed to obtain new insights into the structural characteristics of the serpentine precursor. Hereafter, an accurate model for chrysotile structuration is proposed.

MATERIALS AND METHODS

Experimental synthesis

Semi-continuous chrysotile syntheses were conducted at 300 °C and saturated pressure ($\approx$79 bar) respecting serpentine stoichiometry (Mg/Si = 1.33); starting with 300 mL of 1 M NaOH solution, 1.302 g of silica gel (H_2SiO_3) and 5.082 g of magnesium chloride hexahydrate ($MgCl_2 \cdot 6H_2O$). The reactants were placed in a hastelloy C22 reactor (autoclave with an internal volume of 0.6 L). The suspension was immediately stirred and heated using constant mechanical agitation (300 rpm) and a heating jacket adapted to the reactor as early described in Lafay et al. (2013). Six samples were collected from 10 mL dispersions sampled approximately every half hour, between 40 min and 3 h of reaction. After centrifugation and fluid removal, the solid product was dried at 90 °C during 48 h and recovered for further thermogravimetric analyses (TGA), TEM, and high-energy X-ray diffraction measurements.

A synthetic brucite was produced by reacting 0.25 mol of magnesium chloride hexahydrate in 250 mL of 1 M NaOH solution. Minerals consists in pure $Mg(OH)_2$ hexagonal flakes with a size ranging from few dozens of nanometers to few hundreds of nanometers and a width of about 20 nm.

Solid product characterization

Solid products were characterized by differential thermal analysis (DTA) and TGA with a TGA/SDTA 851e Mettler Toledo instrument using about 10 mg of powder placed in a platinum crucible of 150 μL with a pinhole. Analyses were performed using a heating rate of 10 °C/min, and inert N_2 atmosphere of 50 mL/min. Sample mass loss and associated thermal effects were obtained by TGA/DTA in a temperature range from 30 to 1200 °C. The instrumental theoretical T precision is ±0.5 °C and the weight sensitivity down to 0.1 μg. TGA apparatus was calibrated in terms of mass and temperature. Calcium oxalate was used for the sample mass calibration. The melting points of three compounds (indium, aluminum, and copper) obtained from the DTA signals were used for the sample temperature calibration. The TGA first derivative (so-called differential thermogravimetry DTG) was used to better identify mass loss steps and to determine the loss of mass associated with brucite and serpentine phases (Viti 2010; Lafay et al. 2013; Bloise et al. 2015).

Additionally, samples were loaded into kapton capillaries for high-energy synchrotron X-ray diffraction measurements (HEXD). HEXD experiments allow recording a long momentum transfer (Q) diffraction pattern, including good statistics for the diffuse scattering. These patterns are usually called "total scattering patterns." Total scattering experiments are usually performed to study the local order of amorphous or poorly crystalline materials, where the diffuse scattering accounts for a high proportion of the total X-ray scattering. HEXD patterns of amorphous or disordered materials are usually analyzed using the Pair distribution function [PDF or $g(r)$] approach. In short, the PDF is the Fourier transform of the reduced structure factor, $F(Q)$:

$$F(Q) = Q[S(Q) - 1] \qquad (1)$$

$$g(r) - 1 = \frac{1}{2\pi^2 r\rho} \int_0^\infty Q\left[S(Q) - 1\right]\sin(Qr)\, dr \qquad (2)$$

where r is the interatomic distance, ρ is the number density, and $S(Q)$ is the structure factor. The resulting PDF is a map of the interatomic distances in the sample. The PDF method provides a different way to analyze short-range order, using a real space representation of the scattering data. The PDF method has been use to describe the first stages of formation inorganic materials and the structure of poorly crystalline minerals (Becker et al. 2010; Caraballo et al. 2015; Fernandez-Martinez et al. 2010; Gilbert et al. 2004; Michel et al. 2007). Given the high amount of diffuse scattering present in the diffraction pattern of disordered minerals and of mineral precursors, the PDF provides a useful way to describe the structural characteristics of these phases.

Total scattering patterns were acquired at beamline ID15B of the European Synchrotron Radiation Facility (ESRF), Grenoble, France. Scattering data were collected with a Perkin-Elmer flat-panel detector using the rapid-acquisition pair distribution function (PDF) technique (Chupas et al. 2003). Measurements of the samples and empty capillary were made at ambient temperature in a range of Q from 0–25 Å^{-1}. The X-ray wavelength ($\lambda = 0.14252$ Å) was refined using a NIST certified CeO_2 standard. Total scattering structure functions and pair distribution functions were obtained using the PDFGetX3 software.

TEM was used to determine the shape and sizes of chrysotile nanotubes and of their precursors. For that purpose, powders of samples were dispersed in ethanol and one drop of the sample suspension was deposited on a holey carbon foil placed on conventional copper micro-grids. TEM experiments were performed at the Institut de Minéralogie et de Physique des Milieux et Cosmochimie (Paris, France) using a JEOL 2100F microscope operating at 200 kV, equipped with a field emission gun and a high-resolution pole piece achieving a point-to-point resolution of 1.8 Å, and at Cinam (Marseille, France) using a JEOL 3100 microscope operating at 300 kV equipped with a LaB$_6$ filament achieving a point-to-point resolution of 1.6 Å.

Structural models for simulations

Models of minerals structures were used to simulate PDFs and interpret experimental observations. For that purpose we created atomistic models of chrysotile nanotubes by rolling lizardite layers along the [010] direction, and using average diameter dimensions obtained from TEM images, of 7 and 14 nm for the radii of the inner and outer layers, respectively. The curvature of the layers induces slight shortening and lengthening of Si-O and Mg-O interatomic distances. However, maximum values of these distortions remain physically plausible (see Electronic Annex[1]). PDFs and diffraction patterns from these models were calculated using routines from the Diffpy-CMI library (Juhás et al. 2015). Diffraction patterns were calculated using the Debye equation formalism from non-periodic models of the structures (Warren 1969). Isotropic thermal displacement parameters for all atoms were set to 8×10^{-3} Å^2. VESTA (Momma and Izumi 2011) was used to represent the mineral structures used in this study.

EXPERIMENTAL RESULTS

TGA, DTG, and DTA

TGA and DTG/DTA result are summarized in Figure 1 and Tables 1 and 2. All TGA curves are characterized by a continuous weight loss divided in different dehydroxylation steps that show some variations from 1 to 3 h of reaction. The total weight losses at 800 °C for all samples is about 29% for the two first samples and 22–27% for the four last samples (Table 1). The weight loss below 200 °C is attributed to release of molecular water; this value remains higher than ~9% [usually lower than 5% for pure synthetic and natural chrysotile (Falini et al. 2004; Viti 2010; Lafay et al. 2014b)] suggesting a high water retention by a porous material. The main weight loss occurs in the 200–800 °C range showing a single or double stage, i.e., two distinct DTG

maxima (Table 2) that can be linked to brucite and serpentine dehydroxylation. Before 1 h 30 min of reaction, DTG curves are characterized by a peak at a temperature comprised between 250 and 400 °C related to the decomposition of brucite particles (Blaauw et al. 1979; Wang et al. 1998). Dehydroxylation peak for brucite completely disappears after 2 h of reaction. Note that in previous experiments brucite was clearly observed up to 4 h of reaction (Lafay et al. 2013). However we found relicts of brucite after 3 h of reaction (see TEM measurements section). The time-discrepancy for brucite disappearance could be due to the use of different reactors, implying different vessel material and different volume. After 1 h 30 min a clear dehydroxylation event appears at 537 °C (Fig. 1c) linked to a weak endothermic peak at 541 °C (Table 1). The development of a strong endothermic peak between 2 h and 2 h 50 min of reaction corresponds to the decomposition of particles from the serpentine group (Cattaneo et al. 2003). Here, the weight loss relative to serpentine destabilization (400–700 °C) for the two lasts samples remain in the 11.5–14% range and is consistent with theoretical water content for serpentine minerals. The DTG peak splits after 2 h 25 min of reaction (one component centered at 535 °C and one at 460 °C, Table 2, Fig. 1e) underlying the presence of two kinds of particles or representing the breakdown stage of distinct inner and outer OH groups (Franco et al. 2006). Additionally, the endothermic DTA peak shifts to higher temperature (553 °C, Fig. 1d). After 2 h 50 min of reaction the DTG doublet remains present and linked to DTA endothermic doublet. However the main weight loss component centered at ca. 554 °C (Fig. 1f) supports the presence of a dominant serpentine component.

Since the beginning of the reaction (i.e., after only 40 min of reaction) an exothermic peak is observed in the DTA curves in the 670–715 °C range with an onset oscillating between 640 and 660 °C (except after 1 h, peak at 634 °C). The peak position does not match with the typical temperature of ca. 820 °C sharp exothermic peak related to the crystallization of the remaining amorphous anhydrous meta-chrysotile ($Mg_3Si_2O_7$) into forsterite (Mg_2SiO_4) (Viti 2010). However, we relate this peak to the process of end of dehydration and massive crystallization of forsterite and enstatite. The shift of exothermic DTA peak toward lower temperature referring to pure serpentine in longer experiments (Table 1) might be due to a combination of the difference in shape, size, and density of particles obtained during the first steps of the chrysotile synthesis (Chatzistavrou et al. 2006; Trittschack et al. 2013).

In addition to the reaction pathway described in (Lafay et al. 2013), a more detailed description of the fluctuation observed in the DTA and TGA/DTG curves is given here for the early stages of chrysotile synthesis. We confirmed the presence of brucite in the early stage of the reaction. The oscillating DTG/DTA signal ranging from 200 to 800 °C is linked to a continuous evolution of the abundance, and physical properties of brucite and serpentine-type particles attesting for a non-apparent-equilibrium of the system until 3 h of reaction.

TEM

TEM investigations reveals major changes of particles sizes and morphologies during the first stages of serpentine synthesis until the formation of chrysotile with a typical average width

[1]Deposit item AM-16-125772, Electronic annex. Deposit items are free to all readers and found on the MSA web site, via the specific issue's Table of Contents (go to http://www.minsocam.org/msa/ammin/toc/2016/Dec2016_data/Dec2016_data.html).
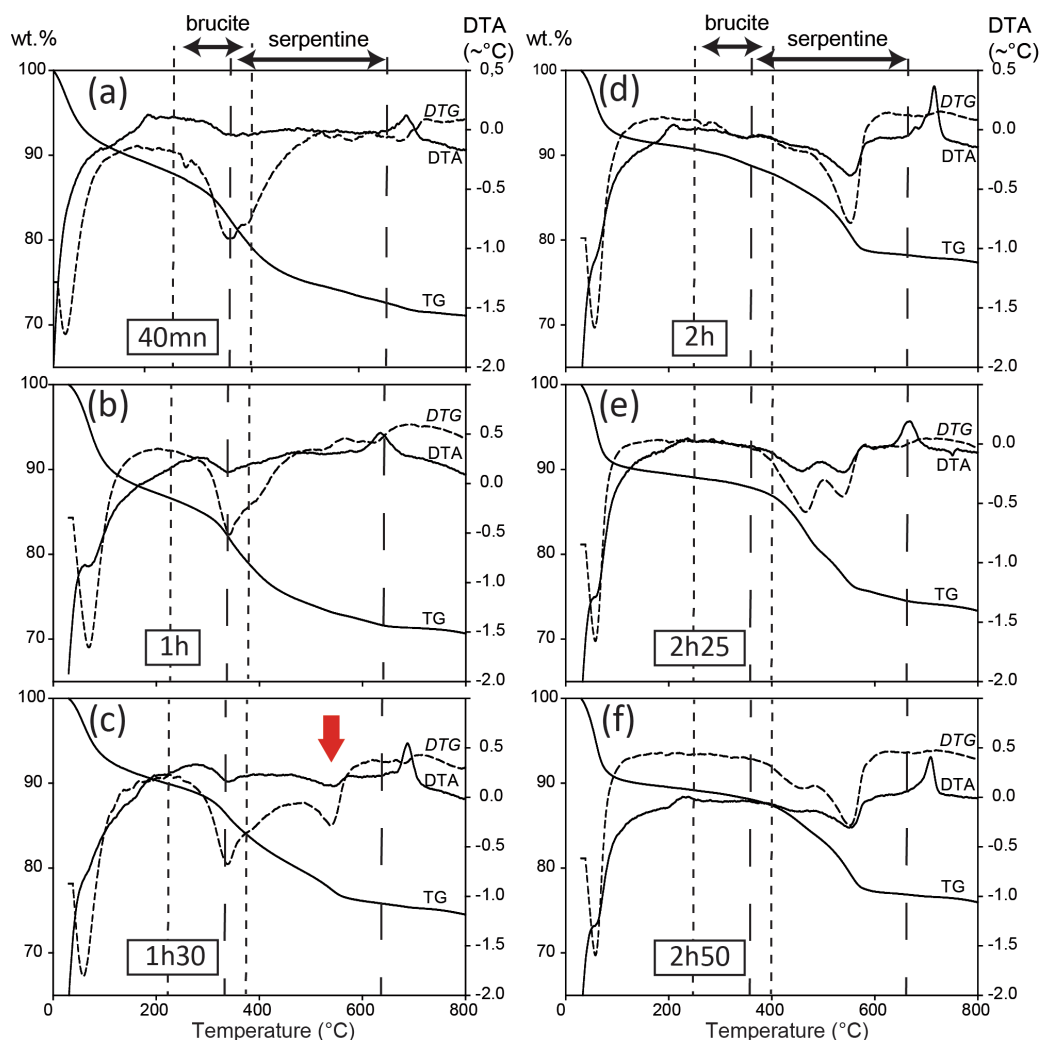
FIGURE 1. Thermal analyses of the sample series performed in N_2 atmosphere: 10 °C/min heating rate and 0–800 °C temperature range. Thermogravimetric losses (TGA) are in wt% and temperature deflection (DTA) are in degrees Celsius. DTG has no unit. Typical dehydroxylation range for brucite and serpentine dehydroxylation are also reported as well as typical serpentine appearance (thick red arrow). (Color online.)

TABLE 1. Summary of TGA weight loss data for samples series

T range (°C)	Reaction time (min) this study						Reaction time (min) Lafay et al. (2013)		
	40	60	90	120	145	170	360	720	1800
	TGA loss (%)								
30–200 α	10.8	12.8	9.7	8.8	10.5	10.5	4.5	5.9	4
200–400 γ	10.3	9.7	7.6	3.4	2.6	2.2	2.7	1.8	1.1
400–800 β	8.5	6.9	8.2	10.5	13.6	11.5	12	11.1	12
sum at 800	29.6	29.4	25.5	22.7	26.7	24.2	19.2	18.8	17.1

Note: Temperature ranges were divided on the base of approximated TGA loss for molecular water (α), brucite mineral (γ), and serpentine group minerals (β).

ranging between 16 and 20 nm and a variable length from 100 to 800 nm. The tunnel width remains extremely monodisperse after 3 h of reaction and is about 7.5–8 nm.

During the first hour of reaction we note the presence of brucite associated with a matrix of flake-like particles constituting an anastomosing network (Figs. 2a and 2b). The presence of brucite in the early steps of the synthesis is consistent with TGA/DTG measurements and previous work (Lafay et al. 2013). The sensitivity of this medium to electron beam made it difficult

to perform TEM characterization with high magnification. After 40 min, the medium is already pre-structured, as shown by the dense regions and the diffraction pattern in Figure 2a, which is characterized by few diffraction bands rather than a diffuse illumination signal. However no sharp diffraction spots specific for a satisfying crystal structure were observed. A few tubular fibers (or conical) can be observed, yet their occurrence remains rare. In addition, between 40 min (corresponding to the end of the heating) and 1 h of reaction, the anastomosed features are

TABLE 2. Summary of DTG and DTA peak temperatures for samples series corresponding to curves on Figure 2

Reaction time (min) this study						Reaction time (min) Lafay et al. (2013)		
40	60	90	120	145	170	360	720	1800
For DTG peak T °C								
277 w	344 ss	338 ss						
363 ss	391 sh	386 sh		460 ss	457 s	366 w		
391 sh	625 w	537 s	553 ss	535 ss	554 ss	593 ss	600 ss	600 ss
584 w								
675 w								
For DTA peak T °C								
687 exo s	335 endo w	341 endo w	555 endo ss	457 endo s	552 endo s	599 endo w	590 endo w	594 endo w
	634 exo s	541 endo w		536 endo s				
		687 exo ss	715 exo ss	670 exo ss	708 exo ss	775 exo ss	814 exo ss	827 exo ss

Note: w = weak, s = strong, ss = very strong (main peak), sh = shoulder, endo = endothermic, exo = exothermic.
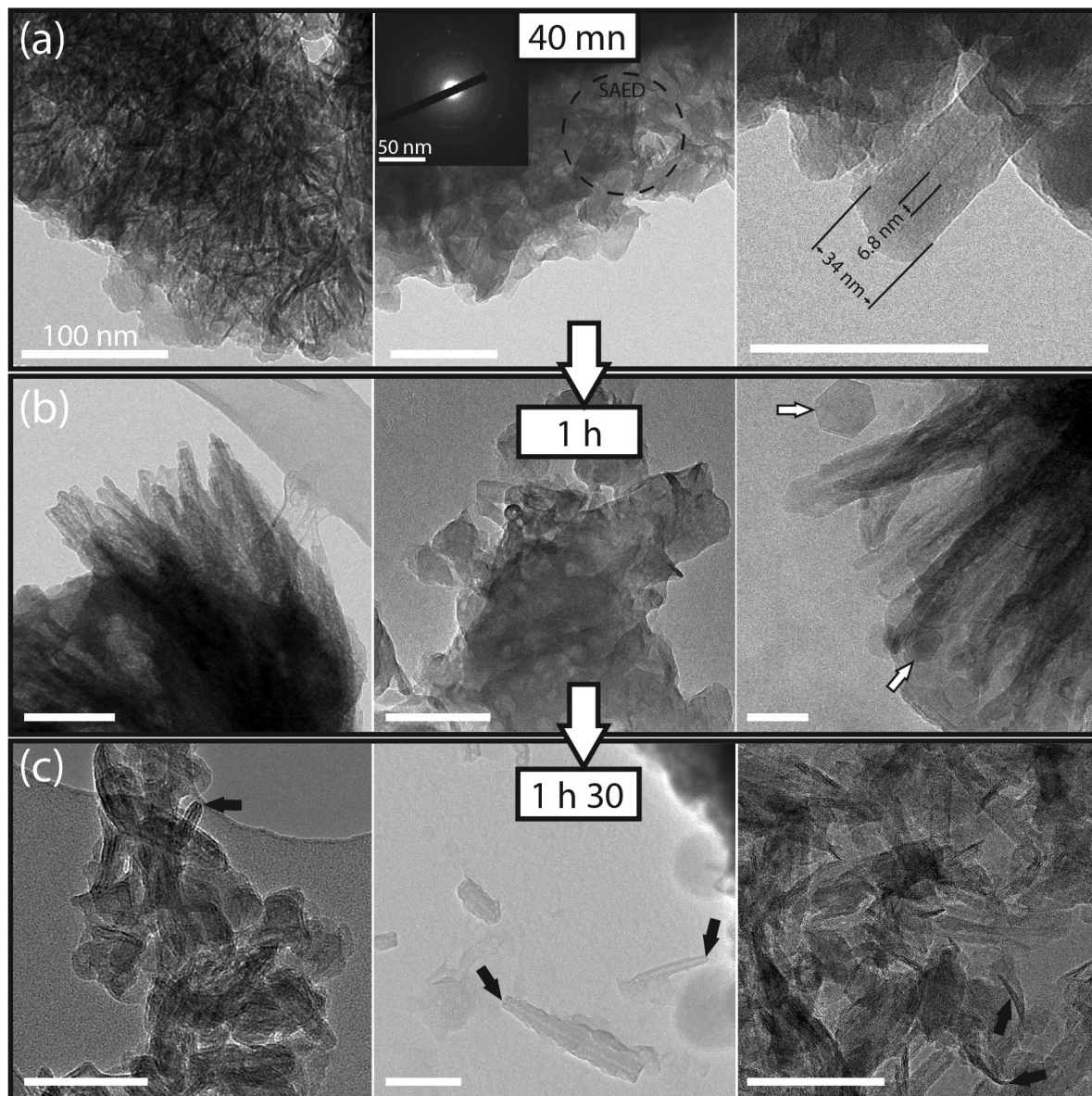

FIGURE 2. Representative samples powder TEM images for several reaction advancements. (**a**) Flake-likes particles (left and middle) and porous anastomosed medium with rare thick individual tubular or conical fibers (right) after 40 min, the selected-area electron diffraction is surrounded, (**b**) fibers likes serpentine particles self-assembly (left and right) and few individual nanotubes (center) with individual brucite (indicated by the white arrows) after 1 h, (**c**) disoriented serpentine nanorods and individual poorly crystallized nanotubes after 1 h and half [black arrows pin-pointed the beveled termination (conical) of serpentine particles]. The scale bar corresponds to 100 nm.

replaced by a porous medium with large fiber-like morphologies as a result of particle aggregation (see Fig. 2b). These fiber-like aggregates display wide (up to 100 nm) and variable diameters and are poorly structured with respect to typical synthetic chrysotile (maximum ~20 nm diameter). In this highly energetic system, heterogeneous particles probably tend to reach a greater structuration and homogenization to lower the misfit energy. The number of manifested individual tubes increase with respect to experiment after 40 min.

After 1 h 30 min of reaction the presence of individual particles is clearly visible and two kinds of crystallites can be distinguished; small flakes coexisting with individual nanotubes, characterized by various sizes and morphology (Fig. 2c). Only few tubes have the typical width and length of the chrysotile reference (which is taken at the end of the reaction). Most of them are smaller than 100 nm in length and they exhibit beveled edges and ovoid shapes like nanorods.

Between 2 h and 2 h 25 min of reaction individual chrysotile with characteristic widths smaller than 20 nm are observed (Fig. 3a). The apparent different width of nanotubes walls might correspond to a difference in phyllosilicate sheets layers and/or atomic density. After 2 h 50 min of reaction, well-crystalized individual nanotubes with thin walls become the dominant species (Fig. 3b). This chrysotile type corresponds to the typical end-member minerals observed after long synthesis experiments (Lafay et al. 2013). As mentioned before, the apparent absence of brucite regarding the TGA signal is due to the presence of only rare relicts of brucite (Fig. 3b). At this point, the chrysotile

morphology can be considered as an equilibrium morphology that lowers the energy due to the mismatch between octahedral and tetrahedral sheets of serpentine in the MgO-SiO$_2$-H$_2$O system (pure Mg system). The occurrence of a double DTG/DTA signal after 2 h 25 min of reaction is consistent with TEM observations underlying the presence of two kinds of chrysotile particles around 2 h of reaction.

High-energy X-ray diffraction and pair distribution function analysis

Structure factors, S(Q), obtained from high-energy X-ray diffraction experiments and the corresponding PDFs of the synthetic samples and synthetic brucite are presented in Figure 4. The most striking characteristic is the fact that, from the beginning of the experiment, all the S(Q) and PDFs show similar features. As expected from TGA and TEM characterization, brucite is present in the samples taken before 1 h 30 min, and its diffraction peaks can be distinguished in the form of a shoulder in the diffraction peak at ~2.45 Å^{-1}. After 1 h 30 min of reaction all the S(Q) and PDFs reveal features common to that of the chrysotile end-member.

An interesting evolution of the low Q peaks is observed (see Fig. 4b). The (004) diffraction peak, at 1.7 Å^{-1}, is only observed after 1 h 30 min. Note that this notation corresponds to the lizardite planar structure (Mellini 1982; Auzende et al. 2006), which has been used to create chrysotile atomistic models; the c axis corresponds to the stacking along the radial direction of the nanotubes. Analysis of the PDFs (Fig. 4c) gives information about the evolution of the coherent domain size, and, again, about
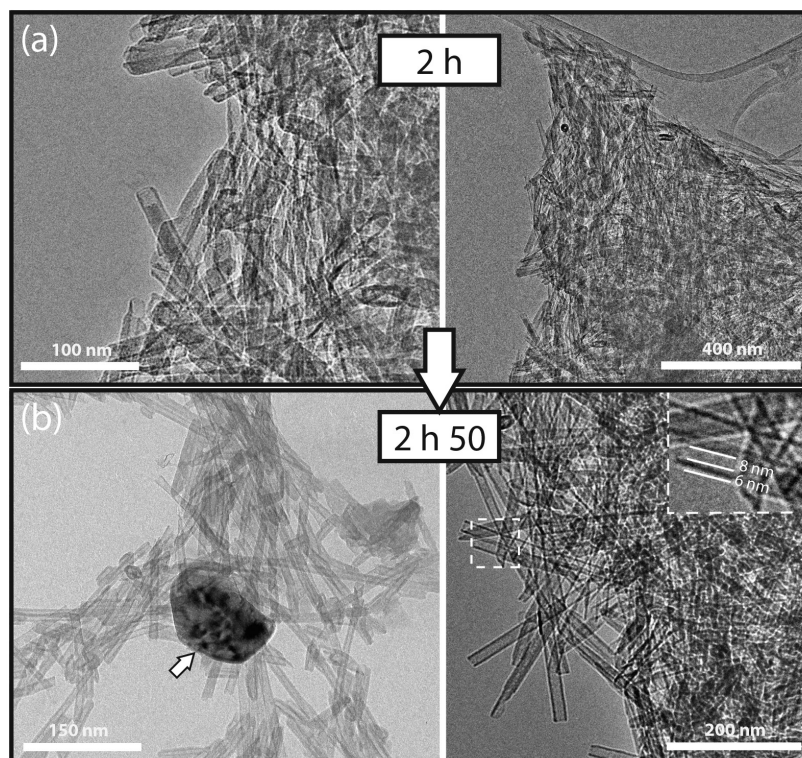

FIGURE 3. Representative samples powder TEM images of individual nanotubes after 2 h (**a**) and 2 h 50 min (**b**) of reaction, typical width of chrysotile tunnel (8 nm) and wall (6 nm) is indicated in right-corner enlarged view, relicts of brucite is pin-pointed by the arrow.
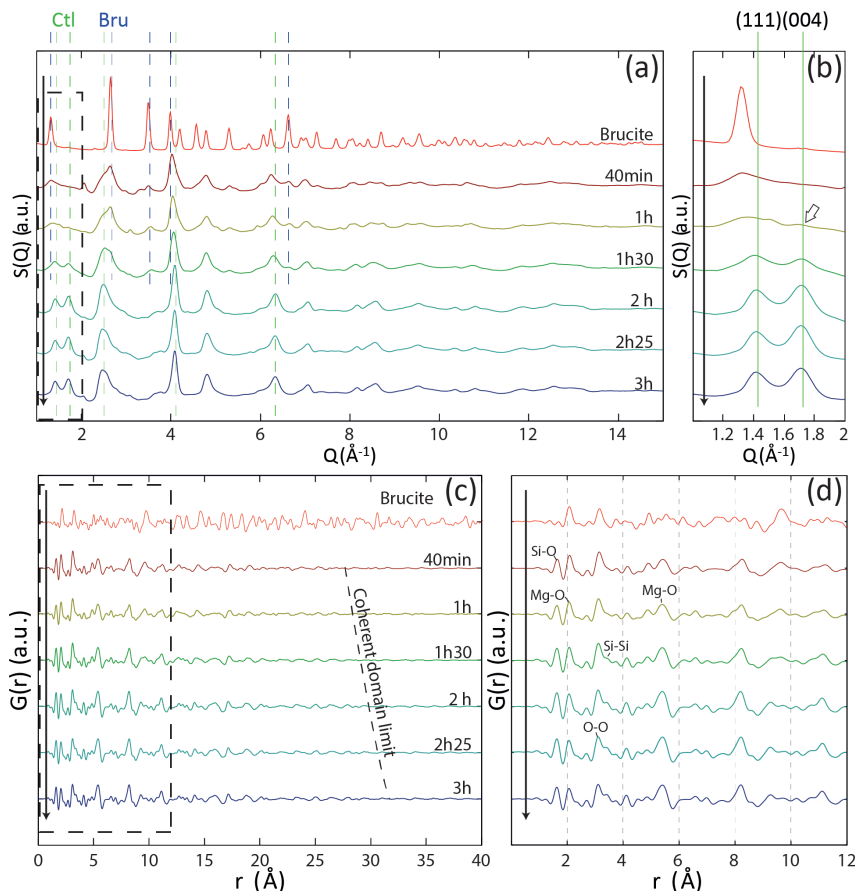
FIGURE 4. (**a**) Experimental structure factor patterns for different reaction advancements. Low-Q region is enlarged in **b** (1.2–2 Å⁻¹ range), with the (004) diffraction peak indicated by the white arrow. Brucite and the chrysotile end-member (3 h of reaction) are reported as references. (**c**) Pair distribution functions (PDFs) of experimental products at different reaction times. The first 10 Å are enlarged in **d**. (Color online.)

the presence of brucite. The decaying intensity of the inter-atomic correlations at long distances is due to a coherent domain size effect, which changes slightly from ~27 Å at 40 min up to 32 Å for the chrysotile obtained after 2 h 50 min. The relatively small increase in the coherent domain size for experimental product is probably due to the existence of defects formed during minerals structuration.

The structuration of chrysotile particles is accompanied by an increase of the Si-O and Si-Si bond intensity in the PDFs (Fig. 4d). We used synthetic brucite and synthetic chrytoile obtained after 3 h of reaction as end-members to fit all the intermediate PDFs. Note here that the PDFs for chrysotile after 2 h 50 min and 30 h of reactions (Lafay et al. 2013) are identical. All patterns can be fitted using a linear combination between two end-members (see Fig. 5). Here the brucite component is not significant and is no longer required after 1 h 30 min of reaction. This result indicates that the chrysotile local order is already present in the samples at early stages of crystallization and that, after 1 h 30 min of reaction, the chrysotile end-member PDF is enough to fit experimental PDFs results.

Additionally, simulations of the evolution of the low-Q part of experimental S(Q) curves (Figs. 4a and 4b) have been performed

by creating chrysotile nanotube structures formed by one, two or four concentric walls (Fig. 6). The simulations reveal that the peak at ~1.7 Å⁻¹, corresponding to the (004) reflection in lizardite, increases proportionally to the number of concentric stacked layers. The structure factor of experimental products after 40 min of reaction displays no features characteristic for multi-wall nanotubes. After 1 h and 1 h 30 min the experimental S(Q) match with a model of two concentric wall layers. Between 1 h 30 min and 2 h of reaction the serpentine products acquire the characteristic features for a coherent concentric stacking of at least four serpentine-sheets. The structure factor does not change anymore after 2 h of reaction. Note that the only way to reproduce the peak intensity is the stacking of concentrical curved lizardite sheets. Tests using physical mixing of single-walled particles with different diameters never reproduced the low Q level of intensity observed for well-crystallized chrysotile.

DISCUSSION AND IMPLICATIONS

Serpentinitization of ultramafic rocks is a widespread hydration reaction that takes place from subsurface lithospheric environment to deep subduction zones and considerably affects rheological and chemical properties of peridotite rocks. It is known that fluid
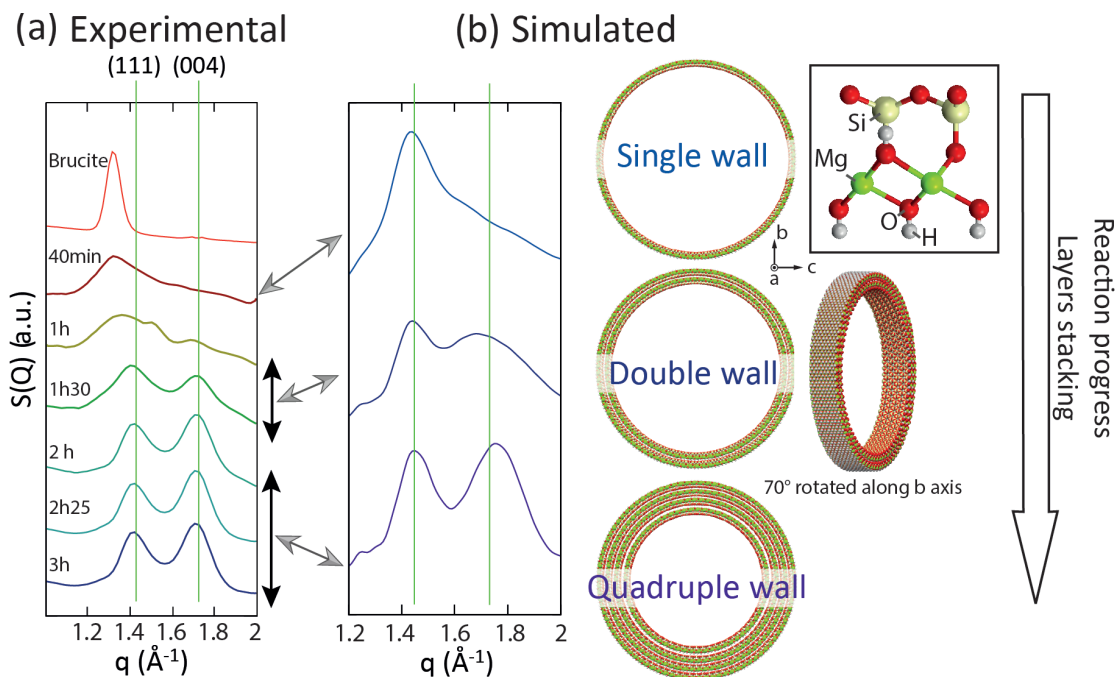
FIGURE 5. (**a**) Enlarged view of the low-q part of the experimental structure factor from Figure 4b, and (**b**) examples of modeled structure factors with the corresponding atomistic structures (including single and multi-walled tubes), built from a lizardite structure (inset). (Color online.)
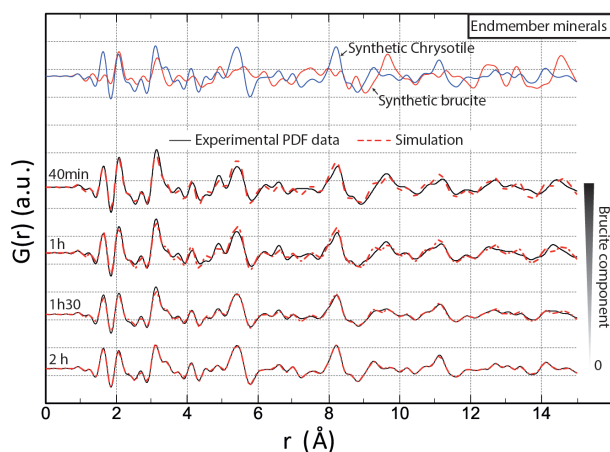

FIGURE 6. Experimental PDFs of samples taken at different reaction advancement from Figure 4c (solid lines) and best fits from the linear combination (dotted lines) using brucite and chrysotile (reference after 2 h 50 min of reaction) as the two mineral end-members. The evolution of the brucite component used for the simulations is also reported. For more detail refer to the text. (Color online.)

circulation in natural environments contributes to large-scale mass transfer and Mg/Si ratio changes during serpentinitization (Niu 2004; Boschi et al. 2006). Pristine mineral alteration involves a dramatic decrease of rock density and rock strength (Escartin et al. 2001). Moreover, rock hydration processes induce small-scale chemical redistributions and important element entrapment (e.g., B, Li, Cl, As, Sb) likely to be released or exchanged during serpentine phase transformation-recrystallization (Vils et al. 2011)

and serpentine dehydration in convergent zones (Deschamps et al. 2013). Some aqueous species greatly increase serpentinization rate in hydrothermal systems and various physicochemical parameters may affect serpentine mineralogical properties (Korytkova et al. 2011; Andreani et al. 2013; Lafay et al. 2014a). Prior to serpentine formation, proto-serpentine has already been described as an amorphous material or "matrix" in natural samples (Plümper et al. 2014). In most studies, proto-serpentine is designated as a poorly crystallized and poorly organized serpentine aggregate from which other serpentine varieties start to growth (Andreani et al. 2008), with a fibrous microstructure (Dufaud et al. 2009; Ryu et al. 2011).

The structural transformation at atomic scale, from serpentine precursor to serpentine end-members, in the MgO-SiO$_2$-H$_2$O system account for small-scale mass transfer at mineral scale during olivine and pyroxene alteration. The study of chrysotile structuring from free-fluid in experimental system—which can been linked to serpentine veins in natural systems (Andreani et al. 2004)—enables the exploration of the progressive serpentine physical properties changes and might account for small-scale chemistry changes and mobile element migration in serpentine veins (Benton et al. 2004).

The results from these analyses dismiss the hypothesis of a totally amorphous material. In many studies, chrysotile is considered as a metastable variety characterizing the first steps of serpentine crystallization, and later re-crystallizing into polygonal serpentine and lizardite (Grauby et al. 1998). In this study, we have focused only on the first part of this process, with chrysotile being the final end-member of the reaction, considered as a reference.

We confirmed that the formation of homogeneous chrysotile is preceded by a stage where transitory phases are rapidly consumed and transformed at least partly by dissolution-precipitation pro-

cesses to supply chrysotile growth. Such assumption is supported by (1) the precipitation of transient brucite and serpentine that remains distinguishable by TGA and TEM analyses up to 2 h of reaction; (2) a progressive evolution of mineral phase properties and proportion accompanied by a loss of total water visible by DTG/DTA pattern in the brucite-serpentine dehydroxylation range from 40 min to 2 h of reaction; and (3) the change in particle size from wide to thin fiber-like particles.

An interesting feature from the DTG/DTA data is the important loss of mass related to serpentine minerals before 1 h of reaction, this despite the absence of the typical dehydroxilation peak. This confirms the presence of small heterogeneous flack-type particles not distinguishable by conventional X-ray powder diffraction analyses. However, the short-range structure of chrysotile is already recognizable by PDF analyses after a short reaction time (Figs. 4 and 5). We reinforce the idea that TGA features are extremely sensitive to the presence of dissolution-precipitation processes and the ensuing changes occurring in the intermediate stage of reaction with the formation of transitory phases. The intensity of the dehydroxylation peak appears to be dependent of the stacking properties and the formation of long-range order in the chrysotile precursors. This could translate into a distribution of dehydroxila- tion temperatures leading to the formation of several peaks (Fig. 1e) instead of the single peak generally observed for crystalline chrysotile (Viti 2010; Lafay et al. 2013; Bloise et al. 2015).

High-energy X-ray diffraction measurements (including PDF analyses) coupled with XRD modeling and TEM characterization enables to depict the specific case of chrysotile formation. The different experimental observations converge toward a picture where particles exhibiting chrysotile short-range order are already formed during the first stages of reaction and coexist with brucite (Figs. 2, 4, and 5) and probably other serpentine-type particles (few tiny nanotubes are already present during the incipient reaction). TEM observations after 1 h of reaction show how these particles aggregate forming elongated wide fiber-like shapes. Interestingly, the size of these aggregates is larger than the typical diameters of the final chrysotile tubes (see Fig. 2b). This could be an indica- tor for the formation of an intermediate meso-structure that is later affected by dissolution-(re)precipitation and structuration processes. The nanoscopic character of these nano-crystalline flake-like particles suggests that they contain a large proportion of edge sites, with -OH groups of variable reactivity.

For a reaction times greater than 1 h 30 min, an increase of the intensity of the diffraction peak along the stacking direction is observed, which can be explained by an increase in stacking of serpentine sheets and the structuration of chrysotile with a multi-wall structure (Fig. 6). This coincides with the observation of individual nanorods and the first visible structured nanotubes. We estimate that before 1 h of reaction, the possible existence of structured nanotubes (i.e., coherent concentric serpentine sheets) remains too small to be distinguishable by high-energy X-ray diffraction measurements. Obviously, after 1 h 30 min the system remains heterogeneous, but previously observed poorly structured nano-fibers tend to be replaced by short nanotubes (nanorods) and individual nanotubes (Fig. 2c). This observation is consistent with the appearance of the typical serpentine dehydroxylation peak in the DTG/DTA pattern. In the final stage, a continuous structuring through stacking of coherent serpentine-sheets (Fig. 5) and the
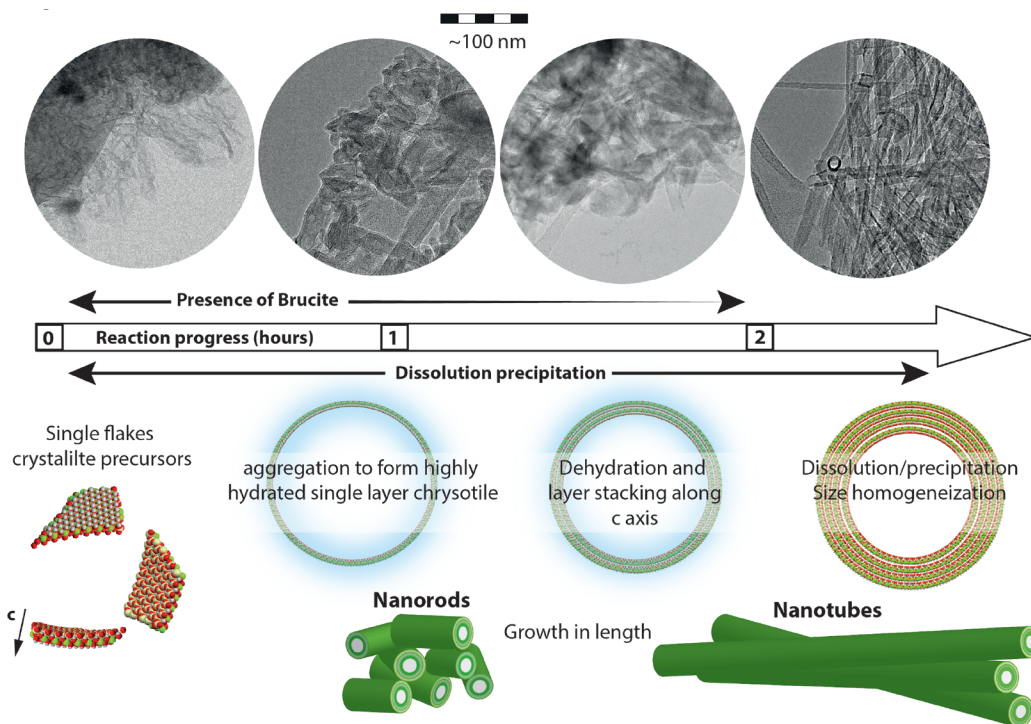

FIGURE 7. Proposed conceptual model for chrysotile nucleation and growth mechanisms. From left to right, structure evolution starts from single nano-sheets of serpentine, initial dissolution-reprecipitation is accompanied by aggregation and stacking along c axis and size homogenization to form nanorods then monodisperse nanotubes assemblage (the schematic representation is not to scale). (Color online.)

formation of longer tubes (Fig. 3) is observed with only minor changes in the diffraction patterns.

In addition to the dissolution-precipitation processes previously discussed, we postulate that the kinetic sequence goes from a disordered pre-structured gel phase with numerous nucleation centers (Fig. 1a) that evolves through time, to a high-energy fiber-like morphologies with various diameters and forms (tubular, flake-like, and conical). We propose that the tubular geometry observed with monodisperse diameter can be considered as the equilibrium morphology for the present conditions and chemical system. Several clues suggest that transformation observed here are inadequate with later chrysotile to lizardite transition proposed from previous experimental studies (Grauby et al. 1998) and mineralization occurring in natural systems.

Our identification of pre-formed short-range ordered particles also support a mechanism of self-assembly or aggregation-based growth (Fig. 7) to minimize energy. This mechanism of particle-attachment has now been identified in various synthetic, biogenic, and geologic environments (De Yoreo et al. 2015). Aggregation and oriented attachment of pre-formed nanoparticles have been reported to be active mechanisms of other common mineral formation such like goethite (Banfield et al. 2000; Guyodo et al. 2003), ferrihydrite (Li et al. 2012), magnetite (Baumgartner et al. 2013), or gypsum (Stawski et al. 2016; Van Driessche et al. 2012), to name the most representative ones. This mechanism is comparable to the one proposed for the structuration of imogolite (Levard et al. 2010), another tubular mineral variety. However, while geological contexts are varied, few studies have addressed hydrothermal conditions due to the difficulty associated with their study. Here, we show an ex-situ study of hydrothermal growth of serpentine from a proto-serpentine precursor.

At an advanced stage of crystallization, after brucite consumption, the presence of Ostwald ripening processes cannot be neglected. The present results provide a way to address the role of this aggregation process in the incipient formation of serpentine in natural systems. The differentiation toward other serpentine varieties remains to be explored. For that purpose, further investigations under different physicochemical parameters (e.g., temperature, pressure, impurities, CO_2/H_2O activity) are on going to ascertain the mechanisms of formation of other serpentine varieties such as lizardite and antigorite. It should be noted that the proficiency to understand the structuration mechanism of nanomaterials remains of great interest for example in applied physics for single- or multi-wall carbon nanotube synthesis (Martel et al. 1998).

REFERENCES CITED

Andreani, M., Baronnet, A., Boullier, A.-M., and Gratier, J.-P. (2004) A microstructural study of a "crack-seal" type serpentine vein using SEM and TEM techniques. European Journal of Mineralogy, 16, 585–595.
Andreani, M., Grauby, O., Baronnet, A., and Muñoz, M. (2008) Occurrence, composition and growth of polyhedral serpentine. European Journal of Mineralogy, 20, 159–171.
Andreani, M., Daniel, I., and Pollet-Villard, M. (2013) Aluminum speeds up the hydrothermal alteration of olivine. American Mineralogist, 98, 1738–1744.
Auzende, A.-L., Pellenq, R. J.-M., Devouard, B., Baronnet, A., and Grauby, O. (2006) Atomistic calculations of structural and elastic properties of serpentine minerals: the case of lizardite. Physics and Chemistry of Minerals, 33, 266–275.
Banfield, J.F., Welch, S.A., Zhang, H., Ebert, T.T., and Penn, R.L. (2000) Aggregation-based crystal growth and microstructure development in natural iron oxyhydroxide biomineralization products. Science, 289, 751–754.
Baumgartner, J., Dey, A., Bomans, P.H. Le Coadou, C., Fratzl, P., Sommerdijk, N.A., and Faivre, D. (2013) Nucleation and growth of magnetite from solution. Nature Materials, 12, 310–314.
Becker, J., Bremholm, M., Tyrsted, C., Pauw, B., Jensen, K.M.O., Eltzholt, J., Christensen, M., and Iversen, B.B. (2010) Experimental setup for in situ X-ray SAXS/WAXS/PDF studies of the formation and growth of nanoparticles in near-and supercritical fluids. Journal of Applied Crystallography. International Union of Crystallography, 43, 729–736.
Benton, L.D., Ryan, J.G., and Savov, I.P. (2004) Lithium abundance and isotope systematics of forearc serpentinites, Conical Seamount, Mariana forearc: Insights into the mechanics of slab-mantle exchange during subduction. Geochemistry, Geophysics, Geosystems, 5.
Blaauw, C., Stroink, G., Leiper, W., and Zentilli, M. (1979) Crystal-field properties of Fe in brucite Mg(OH)$_2$. Physica status solidi (b), 92, 639–643.
Bloise, A., Belluso, E., Barrese, E., Miriello, D., and Apollaro, C. (2009) Synthesis of Fe-doped chrysotile and characterization of the resulting chrysotile fibers. Crystal Research and Technology, 44, 590–596.
Bloise, A., Belluso, E., Catalano, M., Barrese, E., Miriello, D., and Apollaro, C. (2012) Hydrothermal alteration of glass to chrysotile. Journal of the American Ceramic Society, 95, 3050–3055.
Bloise, A., Catalano, M., Barrese, E., Gualtieri, A.F., Gandolfi, N.B., Capella, S., and Belluso, E. (2015) TG/DSC study of the thermal behaviour of hazardous mineral fibres. Journal of Thermal Analysis and Calorimetry, 1–15.
Boschi, C., Früh-Green, G.L., Delacour, A., Karson, J.A., and Kelley, D.S. (2006) Mass transfer and fluid flow during detachment faulting and development of an oceanic core complex, Atlantis Massif (MAR 30 N). Geochemistry, Geophysics, Geosystems, 7.
Caraballo, M.A., Michel, F.M., and Hochella, M.F. (2015) The rapid expansion of environmental mineralogy in unconventional ways: Beyond the accepted definition of a mineral, the latest technology, and using nature as our guide. American Mineralogist, 100, 14–25.
Cattaneo, A., Gualtieri, F., and Artioli, G. (2003) Kinetic study of the dehydroxylation of chrysotile asbestos with temperature by in situ XRPD. Physics and Chemistry of Minerals, 30, 177–183.
Chatzistavrou, X., Zorba, T., Chrissafis, K., Kaimakamis, G., Kontonasaki, E., Koidis, P., and Paraskevopoulos, K.M. (2006) Influence of particle size on the crystallization process and the bioactive behavior of a bioactive glass system. Journal of Thermal Analysis and Calorimetry, 85, 253–259.
Chupas, P.J., Qiu, X., Hanson, J.C., Lee, P.L., Grey, C.P., and Billinge, S.J. (2003) Rapid-acquisition pair distribution function (RA-PDF) analysis. Journal of Applied Crystallography, 36, 1342–1347.
Cressey, B.A., and Whittaker, E.J.W. (1993) Five-fold symmetry in chrysotile asbestos revealed by transmission electron microscopy. Mineralogical Magazine, 57, 729–732.
Cressey, G., Cressey, B.A., Wicks, F.J., and Yada, K. (2010) A disc with fivefold symmetry: the proposed fundamental seed structure for the formation of chrysotile asbestos fibres, polygonal serpentine fibres and polyhedral lizardite spheres. Mineralogical Magazine, 74, 29–37.
Daval, D., Hellmann, R., Corvisier, J., Tisserand, D., Martinez, I., and Guyot, F. (2010) Dissolution kinetics of diopside as a function of solution saturation state: Macroscopic measurements and implications for modeling of geological storage of CO_2. Geochimica et Cosmochimica Acta, 74, 2615–2633.
Daval, D., Hellmann, R., Saldi, G.D., Wirth, R., and Knauss, K.G. (2013) Linking nm-scale measurements of the anisotropy of silicate surface reactivity to macroscopic dissolution rate laws: New insights based on diopside. Geochimica et Cosmochimica Acta, 107, 121–134.
De Yoreo, J.J., Gilbert, P., Sommerdijk, N., Penn, R.L., Whitelam, S., Joester, D., Zhang, H., Rimer, J.D., Navrotsky, A., and others. (2015) Crystallization by particle attachment in synthetic, biogenic, and geologic environments. Science, 349, 6760.
Deschamps, F., Godard, M., Guillot, S., and Hattori, K. (2013) Geochemistry of subduction zone serpentinites: A review. Lithos, 178, 96–127.
Dufaud, F., Martinez, I., and Shilobreeva, S. (2009) Experimental study of Mg-rich silicates carbonation at 400 and 500 C and 1 kbar. Chemical Geology, 265, 79–87.
Escartin, J., Hirth, G., and Evans, B. (2001) Strength of slightly serpentinized peridotites: Implications for the tectonics of oceanic lithosphere. Geology, 29, 1023–1026.
Evans, B. (2004) The serpentinite multisystem revisited: Chrysotile is metastable. International Geology Review, 46, 479–506.
Evans, B.W., Johannes, W., Oterdoom, H., and Trommsdorff, V. (1976) Stability of chrysotile and antigorite in the serpentinite multisystem. Schweizerische Mineralogische und Petrographische Mitteilungen, 56, 79–93.
Falini, G., Foresti, E., Gazzano, M., Gualtieri, A.F., Leoni, M., Lesci, I.G., and Roveri, N. (2004) Tubular-shaped stoichiometric chrysotile nanocrystals. Chemistry—A European Journal, 10, 3043–3049.
Falini, G., Foresti, E., Lesci, I.G., Lunelli, B., Sabatino, P., and Roveri, N. (2006) Interaction of bovine serum albumin with chrysotile: Spectroscopic and morphological studies. Chemistry—A European Journal, 12, 1968–1974.

Fernandez-Martinez, A., Timon, V., Román-Ross, G., Cuello, G.J., Daniels, J.E., and Ayora, C. (2010) The structure of schwertmannite, a nanocrystalline iron oxyhydroxysulfate. American Mineralogist, 95, 1312–1322.

Foresti, E., Fornero, E., Lesci, I.G., Rinaudo, C., Zuccheri, T., and Roveri, N. (2009) Asbestos health hazard: A spectroscopic study of synthetic geoinspired Fe-doped chrysotile. Journal of Hazardous Materials, 167, 1070–1079.

Franco, F., Pérez-Maqueda, L.A., Ramírez-Valle, V., and Pérez-Rodríguez, J.L. (2006) Spectroscopic study of the dehydroxylation process of a sonicated antigorite. European Journal of Mineralogy, 18, 257–264.

Gilbert, B., Huang, F., Zhang, H., Waychunas, G.A., and Banfield, J.F. (2004) Nanoparticles: Strained and stiff. Science, 305, 651–654.

Godard, M., Luquot, L., Andreani, M., and Gouze, P. (2013) Incipient hydration of mantle lithosphere at ridges: A reactive-percolation experiment. Earth and Planetary Science Letters, 371, 92–102.

Grauby, O., Baronnet, A., Devouard, B., Schoumacker, K., and Demirdjian, L. (1998) The chrysotile-polygonal serpentine-lizardite suite synthesized from a 3MgO-2SiO$_2$-excess H$_2$O gel. The 7th International Symposium on Experimental Mineralogy, Petrology, and Geochemistry, Orléans, Abstracts. Terra Nova, supplement, 24.

Guyodo, Y., Mostrom, A., Lee Penn, R., and Banerjee, S.K. (2003) From Nanodots to Nanorods: Oriented aggregation and magnetic evolution of nanocrystalline goethite. Geophysical Research Letters, 30, 1512.

Hövelmann, J., Austrheim, H., Beinlich, A., and Munz, I.A. (2011) Experimental study of the carbonation of partially serpentinized and weathered peridotites. Geochimica et Cosmochimica Acta, 75, 6760–6779.

James, R.H., Allen, D.E., and Seyfried, W. (2003) An experimental study of alteration of oceanic crust and terrigenous sediments at moderate temperatures (51 to 350 °C): Insights as to chemical processes in near-shore ridge-flank hydrothermal systems. Geochimica et Cosmochimica Acta, 67, 681–691.

Jancar, B., and Suvorov, D. (2006) The influence of hydrothermal-reaction parameters on the formation of chrysotile nanotubes. Nanotechnology, 17, 25–29.

Juhás, P., Farrow, C.L., Yang, X., Knox, K.R., and Billinge, S.J.L. (2015) Complex modeling: a strategy and software program for combining multiple information sources to solve ill posed structure and nanostructure inverse problems. Acta Crystallographica. A71, 562–568.

Korytkova, E., and Pivovarova, L. (2010) Hydrothermal synthesis of nanotubes based on (Mg,Fe,Co,Ni)$_3$Si$_2$O$_5$(OH)$_4$ hydrosilicates. Glass Physics and Chemistry, 36, 53–60.

Korytkova, E., Brovkin, A., Maslennikova, T., Pivovarova, L., and Drozdova, I. (2011) Influence of the physicochemical parameters of synthesis on the growth of nanotubes of the Mg$_3$Si$_2$O$_5$(OH)$_4$ composition under hydrothermal conditions. Glass Physics and Chemistry, 37, 161–171.

Kunze, G. (1956) Die gewellte Struktur des Antigorits, I. Zeitschrift für Kristallographie—Crystalline Materials, 108, 82–107.

Lafay, R., Janots, E., and Montes-Hernandez, G. (2014a) Lithium control on experimental serpentinization processes: implications for natural systems. EGU General Assembly 2014, held 27 April-2 May, 2014 in Vienna, Austria, id. 14295.

Lafay, R., Montes-Hernandez, G., Janots, E., Auzende, A.-L., Chiriac, R., Lemarchand, D., and Toche, F. (2014b) Influence of trace elements on the textural properties of synthetic chrysotile: Complementary insights from macroscopic and nanoscopic measurements. Microporous and Mesoporous Materials, 183, 81–90.

Lafay, R., Montes-Hernandez, G., Janots, E., Chiriac, R., Findling, N., and Toche, F. (2013) Nucleation and growth of chrysotile nanotubes in H$_2$SiO$_3$/MgCl$_2$/NaOH medium at 90 to 300 °C. Chemistry—A European Journal, 19, 5417–5424.

Levard, C., Rose, J., Thill, A., Masion, A. Doelsch, E., Maillet, P., Spalla, O., Olivi, L., Cognini, A. Ziarelli, F., and Bottero, J.-Y. (2010) Formation and growth mechanisms of imogolite-like aluminogermanate nanotubes. Chemistry of Materials, 22, 2466–2473.

Li, D., Nielsen, M.H., Lee, J.R., Frandsen, C., Banfield, J.F., and De Yoreo, J.J. (2012) Direction-specific interactions control crystal growth by oriented attachment. Science, 336, 1014–1018.

Macleod, G., McKeown, C., Hall, A.J., and Russell, M.J. (1994) Hydrothermal and oceanic pH conditions of possible relevance to the origin of life. Origins of Life and Evolution of the Biosphere, 24, 19–41.

Martel, R., Schmidt, T., Shea, H., Hertel, T., and Avouris, P. (1998) Single-and multi-wall carbon nanotube field-effect transistors. Applied Physics Letters, 73, 2447–2449.

McCollom, T.M., and Bach, W. (2009) Thermodynamic constraints on hydrogen generation during serpentinization of ultramafic rocks. Geochimica et Cosmochimica Acta, 73, 856–875.

Mellini, M. (1982) The crystal structure of lizardite 1T: hydrogen bonds and polytypism. American Mineralogist, 67, 587–598.

Michel, F.M., Ehm, L., Antao, S.M., Lee, P.L., Chupas, P.J., Liu, G., Strongin, D.R., Schoonen, M.A.A., Phillips, B.L., and Parise, J.B. (2007) The structure of ferrihydrite, a nanocrystalline material. Science, 316, 1726–1729.

Middleton, A.P., and Whittaker, E. (1976) The structure of povlen-type chrysotile. Canadian Mineralogist, 14, 301–306.

Momma, K., and Izumi, F. (2011) VESTA 3 for three-dimensional visualization of crystal, volumetric and morphology data. Journal of Applied Crystallography, 44, 1272–1276.

Niu, Y. (2004) Bulk-rock major and trace element compositions of abyssal peridotites: Implications for mantle melting, melt extraction and post-melting processes beneath mid-ocean ridges. Journal of Petrology, 45, 2423–2458.

Noll, von, W. (1950) Synthesen im System MgO/SiO$_2$/H$_2$O. Zeitschrift für anorganische Chemie, 261, 1–25.

Pauling, L. (1930) The structure of the chlorites. Proceedings of the National Academy of Sciences, 16, 578.

Plümper, O., Røyne, A., Magrasó, A., and Jamtveit, B. (2012) The interface-scale mechanism of reaction-induced fracturing during serpentinization. Geology, 40, 1103–1106.

Plümper, O., Beinlich, A., Bach, W., Janots, E., and Austrheim, H. (2014) Garnets within geode-like serpentinite veins: Implications for element transport, hydrogen production and life-supporting environment formation. Geochimica et Cosmochimica Acta, 141, 454–471.

Putnis, A. (2002) Mineral replacement reactions: from macroscopic observations to microscopic mechanisms. Mineralogical Magazine, 66, 689–708.

Ryu, K.W., Lee, M.G., and Jang, Y.N. (2011) Mechanism of tremolite carbonation. Applied Geochemistry, 26, 1215–1221.

Seyfried, W.E., and Dibble, W.E. (1980) Seawater-peridotite interaction at 300°C and 500 bars: implications for the origin of oceanic serpentinites. Geochimica et Cosmochimica Acta, 44, 309–321.

Seyfried, W.E., Foustoukos, D.I., and Fu, Q. (2007) Redox evolution and mass transfer during serpentinization: An experimental and theoretical study at 200 °C, 500 bar with implications for ultramafic-hosted hydrothermal systems at Mid-Ocean Ridges. Geochimica et Cosmochimica Acta, 71, 3872–3886.

Stawski, T.M., van Driessche, A.E., Ossorio, M., Rodriguez-Blanco, J.D., Besselink, R., and Benning, L.G. (2016) Formation of calcium sulfate through the aggregation of sub-3 nanometre primary species. Nature Communications, 7, 11177.

Trittschack, R., Grobéty, B., and Koch-Müller, M. (2012) In situ high-temperature Raman and FTIR spectroscopy of the phase transformation of lizardite. American Mineralogist, 97, 1965–1976.

Trittschack, R., Grobéty, B., and Brodard, P. (2013) Kinetics of the chrysotile and brucite dehydroxylation reaction: a combined non-isothermal/isothermal thermogravimetric analysis and high-temperature X-ray powder diffraction study. Physics and Chemistry of Minerals, 41, 197–214.

Turci, F., Tomatis, M., Lesci, I.G., Roveri, N., and Fubini, B. (2011) The iron-related molecular toxicity mechanism of synthetic asbestos nanofibres: A model study for high-aspect-ratio nanoparticles. Chemistry—A European Journal, 17, 350–358.

Van Driessche, A., Benning, L., Rodriguez-Blanco, J., Ossorio, M., Bots, P., and García-Ruiz, J. (2012) The role and implications of bassanite as a stable precursor phase to gypsum precipitation. Science, 336, 69–72.

Velbel, M.A. (1993) Formation of protective surface layers during silicate-mineral weathering under well-leached, oxidizing conditions. American Mineralogist, 78, 405–405.

——— (2009) Dissolution of olivine during natural weathering. Geochimica et Cosmochimica Acta, 73, 6098–6113.

Vils, F., Müntener, O., Kalt, A., and Ludwig, T. (2011) Implications of the serpentine phase transition on the behaviour of beryllium and lithium-boron of subducted ultramafic rocks. Geochimica et Cosmochimica Acta, 75, 1249–1271.

Viti, C. (2010) Serpentine minerals discrimination by thermal analysis. American Mineralogist, 95, 631–638.

Wang, J.A., Novaro, O., Bokhimi, X., Lopez, T., Gomez, R., Navarrete, J., Llanos, M.E., and Lopez-Salinas, E. (1998) Characterizations of the thermal decomposition of brucite prepared by sol-gel technique for synthesis of nanocrystalline MgO. Materials Letters, 35, 317–323.

Warren, B.E. (1969) X-ray Diffraction. Courier Corporation.

Whittaker, E. (1956a) The structure of chrysotile. II. Clino-chrysotile. Acta Crystallographica, 9, 855–862.

——— (1956b) The structure of chrysotile. III. Ortho-chrysotile. Acta Crystallographica, 9, 862–864.

——— (1956c) The structure of chrysotile. IV. Para-chrysotile. Acta Crystallographica, 9, 865–867.

Wicks, F.J., and O'Hanley, D.S. (1988) Serpentine minerals; structures and petrology. Reviews in Mineralogy and Geochemistry, 19, 91–167.

Wicks, F., and Whittaker, E. (1977) Serpentine textures and serpentinization. Canadian Mineralogist, 15, 459–488.

Wunder, B., and Schreyer, W. (1997) Antigorite: High-pressure stability in the system MgO-SiO$_2$-H$_2$O (MSH). Lithos, 41, 213–227.

Yada, K. (1967) Study of chrysotile asbestos by a high resolution electron microscope. Acta Crystallographica, 23, 704–707.

Yada, K., and Iishi, K. (1974) Serpentine minerals hydrothermally synthesized and their microstructures. Journal of Crystal Growth 24– 25, 627–630.

——— (1977) Growth and microstructure of synthetic chrysotile. American Mineralogist, 62, 958–965.